International Journal of Thermal Sciences 116 (2017) 265–277

Contents lists available at ScienceDirect

International Journal of Thermal Sciences

journal homepage: www.elsevier.com/locate/ijts

Frequency-domain optical tomographic image reconstruction algorithm with the simplified spherical harmonics (SP_3) light propagation model

Hyun Keol Kim [a, *], Ludguier D. Montejo [b], Jingfei Jia [b], Andreas H. Hielscher [a, b, c, **]

[a] Department of Radiology, Columbia University, 660 W 168th St, New York, NY 10327, USA
[b] Department of Biomedical Engineering, Columbia University, 500 W 120th St, New York, NY 10027, USA
[c] Department of Electrical Engineering, Columbia University, New York, NY 10027, USA

ARTICLE INFO

Article history:
Received 1 August 2016
Received in revised form
1 December 2016
Accepted 4 March 2017
Available online 18 March 2017

Keywords:
Radiative transfer
Simplified spherical harmonics
Image reconstruction
Biological tissue

ABSTRACT

We introduce here the finite volume formulation of the frequency-domain simplified spherical harmonics model with *n*-th order absorption coefficients (FD-SP_N) that approximates the frequency-domain equation of radiative transfer (FD-ERT). We then present the FD-SP_N based reconstruction algorithm that recovers absorption and scattering coefficients in biological tissue. The FD-SP_N model with 3rd order absorption coefficient (i.e., FD-SP_3) is used as a forward model to solve the inverse problem. The FD-SP_3 is discretized with a node-centered finite volume scheme and solved with a restarted generalized minimum residual (GMRES) algorithm. The absorption and scattering coefficients are retrieved using a limited-memory Broyden-Fletcher-Goldfarb-Shanno (L-BFGS) algorithm. Finally, the forward and inverse algorithms are evaluated using numerical phantoms with optical properties and size that mimic small-volume tissue such as finger joints and small animals.

The forward results show that the FD-SP_3 model approximates the FD-ERT (S_{12}) solution within high accuracy; the average errors in the phase (<3.7%) and the amplitude (<7.1%) of the partial current at the boundary are reported. From the inverse results we find that the absorption and scattering coefficient maps are more accurately reconstructed with the SP_3 model than those with the SP_1 model. Therefore, this work shows that the FD-SP_3 is an efficient model for optical tomographic imaging of small-volume media with non-diffuse properties both in terms of computational time and accuracy as it requires significantly lower CPU time than the FD-ERT (S_{12}) and also it is more accurate than the FD-SP_1.

1. Introduction

Modeling of light propagation in biological tissue has been extensively studied in biomedical optics over the past several decades. Various models have so far been developed that make use of high-performance computing and new numerical methods. Fundamentally, two different approaches have been pursued: (a) Monte Carlo (MC) modeling [1–3] and (b) numerical solutions to the equation of radiative transfer (ERT) and its approximations [4–15].

The ERT has been shown to be the most accurate deterministic model for the propagation of light in tissue. However, widespread use of the ERT has been limited due to high computational demand with numerical solution. This poses particular challenges in diffuse optical tomography (DOT), where the ERT needs to be solved many times for different source and detector configurations. Thus, depending on the particular clinical or preclinical application, ERT-based image reconstructions may take hours or even days. The main reasons for high computational cost are: 1) the upwind (or step) scheme method, which is the most popular spatial differencing scheme for solving the ERT but only first order accurate, requires dense spatial discretization to improve spatial accuracy; 2) accurate modeling of highly forward scattered light (as is often the case in biological tissue) requires dense angular discretization to accurately capture such highly forward scattering of light in tissue; 3) the presence of scattering makes light intensities at different directions strongly coupled, leading to slow convergence.

* Corresponding author. 622 West 168th Street, New York, NY 10032, USA.
** Corresponding author. 500 West 120th Street, New York, NY 10027, USA.
E-mail addresses: hkk2107@cumc.columbia.edu (H.K. Kim), ahh2004@columbia.edu (A.H. Hielscher).

http://dx.doi.org/10.1016/j.ijthermalsci.2017.03.004
1290-0729/

Altogether, the total number of equations that results from both spatial and angular discretization of the ERT is very large, thus leading to computation times that are often impractical for clinical applications.

As a result of these computational considerations, approximations to the ERT have become increasingly important and common. The most common approximation is the diffusion equation (DE), which assumes that light propagates diffusely through tissue. This assumption is valid only under conditions where light is highly scattered and infrequently absorbed. Thus, the DE is a poor approximation to the ERT in tissue of small volume, with high absorption, or void-like regions [14,16]. This limits the applications for which the DE can be used. For example, some groups (including our team) have recently shown that DOT appears to be capable of accurately diagnosing rheumatoid arthritis (RA) [17–19] and osteoarthritis (OA) [20–22] in finger joints. Yet because fingers contain void-like regions, occupy a relatively small volume, and, in the case of RA, may contain inflamed regions that are highly absorbing, the DE is of limited accuracy.

To improve modeling accuracy, Klose and Larsen introduced the steady-state SP_N model for use in DOT in 2006 [23]. They showed that the SP_N approximation to the ERT is superior to the DE in modeling light propagation in small-volume tissue, with high absorption values, and with low scattering values. A thorough analysis of the model for $N = 1, 3, 5$, and 7 showed that the SP_N model is able to capture the majority of transport behaviors of photons inside biological tissue. Furthermore, it was extensively shown that the SP_3 model provides sufficient improvements over the DE while still providing a significant reduction in computational time as compared to the ERT model.

From a computational point of view, the SP_N equation has a much smaller number of coupled equations than the ERT. Furthermore, the number of computational grid points can be significantly fewer when using the SPN model because from its resulting discretization is second-order accurate, and therefore, the computation mesh does not need to be as dense as the mesh required to accurately solve the ERT [24].

Following a strategy similar to that presented by Klose and Larsen [23], Domínguez and Bérubé-Lauzière derived the time-domain parabolic SP_N (TD-pSP_N) model from the source-divergence time-dependent ERT [25]. From the TD-pSP_N model, the authors also derived the frequency-domain SP_N (FD-SP_N) model for the source-divergence time-dependent ERT. We are, however, interested in the SP_N approximation to the standard frequency domain ERT for use in clinical studies [17–19],

$$\left(\hat{\Omega}\cdot\nabla + \mu_t(r) + \frac{i\omega}{\upsilon}\right)\psi\left(r,\hat{\Omega},\omega\right) = \mu_s(r)\int_{4\pi} p\left(\hat{\Omega}\cdot\hat{\Omega}'\right)\psi\left(r,\hat{\Omega}',\omega\right)d\Omega' + \frac{Q(r,\omega)}{4\pi} \tag{1}$$

$$\psi\left(r,\hat{\Omega},\omega\right) = S\left(r,\hat{\Omega},\omega\right) + R\left(\hat{\Omega}'\cdot\hat{n}\right)\cdot\psi(r,\hat{\Omega}',\omega)_{\hat{\Omega}'\cdot\hat{n}>0},\ r\in\delta V,\ \hat{\Omega}\cdot\hat{n}<0. \tag{2}$$

The SP_N approximation to this ERT model can be obtained by modifying the source-divergence time-dependent ERT model as done in the work by Domínguez and Bérubé-Lauzière. Assuming that the refractive index in the medium is spatially invariant and that the discrete ordinates ($\hat{\Omega}$) are independent from spatial position (i.e. $\nabla_r\cdot\hat{\Omega} = 0$), then a TD-$SP_N$ model can be recovered for the standard time-dependent ERT model. This standard TD-SP_N model can then be used to derive the FD-SP_N approximation to (1) and (2). The model for $N = 3$ is presented below,

$$-\nabla\cdot D_1\nabla\phi_1 + \left(\mu_a + \frac{i\omega}{\upsilon}\right)\phi_1 = \dot{q} + \frac{2}{3}\left(\mu_a + \frac{i\omega}{\upsilon}\right)\phi_2, \tag{3}$$

$$-\nabla\cdot D_2\nabla\phi_2 + \left(\frac{4}{9}\mu_a + \frac{5}{9}\mu_{a2} + \frac{1}{3}\frac{i\omega}{\upsilon}\right)\phi_2 = -\frac{2}{3}\dot{q} + \frac{2}{3}\mu_a\phi_1, \tag{4}$$

where ϕ_1 and ϕ_2 denote composite moments of the fluence in units of Wcm^{-2}, such that the Legendre moments of the radiance are given by $\psi_0 = \phi_1 - 2\phi_2$ and $\psi_1 = 2\phi_2$. The n-th order absorption coefficient is given by $\mu_{a,n} = \mu_a + (1 - g^n)\mu_s$, where μ_a is the absorption coefficient, μ_s is the scattering coefficient, and g is the anisotropy factor ($g\in[0.8,\ 1.0]$ for many biological media [26]). The modulation frequency of the source laser is denoted by ω, υ is the speed of light in the medium, $\dot{q}$ denotes an internal source of light, and $D_1 = (3\mu_{a,1})^{-1}$ and $D_2 = (7\mu_{a,3})^{-1}$. The corresponding set of boundary equations is given as follows:

$$\alpha_1\phi_1 + D_1\beta_1(\hat{n}\cdot\nabla\phi_1) = \gamma_1\phi_2 + 7D_2\delta_1(\hat{n}\cdot\nabla\phi_2) + S_1, \tag{5}$$

$$\alpha_2\phi_2 + D_2\beta_2(\hat{n}\cdot\nabla\phi_2) = \gamma_2\phi_1 + 3D_1\delta_2(\hat{n}\cdot\nabla\phi_1) + S_2. \tag{6}$$

Coefficients $\alpha_1,\ \beta_1, \gamma_1,\ \delta_1,\ \alpha_2,\ \beta_2, \gamma_2$, and δ_2 are defined in Table 1. The FD-SP_N approximation to (1)–(2) given by (3)–(6) differs from the model presented by Domínguez and Bérubé-Lauzière in that the divergence coefficient vanishes in all terms (i.e. $\mu_d(r) = 0$).

A different version of this FD-SP_N model was previously presented by Chu et al. in Ref. [27]; however, that model differs from (3)–(6) in a significant manner. Primarily, the $\mu_{a,n}$ coefficients are strictly real-valued in (3)–(6), whereas the $\mu_{a,n}$ terms in the FD-SP_N model by Chu are complex-valued. One of the main implications of this difference is that the FD-SP_N model given by (3)–(6) converges to the diffusion equation when $N = 1$, while the model by Chu et al. does not.

This difference motivated our efforts to develop a DOT algorithm that is based on (3)–(6). We are interested in this model (3)–(6) because it may prove to be critical in future studies related to imaging of finger joints and other clinical applications with a frequency domain DOT imaging system. To the best of our knowledge, however, this model has not been evaluated for accuracy and performance in frequency-domain DOT. Limited work has been published on image reconstruction with the FD-SP_N model as presented by Chu et al.; for example, Lu et al. published the work on frequency

Table 1
Definitions of coefficients in the FD-SP3 model. The definition of variables A_i, B_i, C_i, D_i, and J_i can be obtained in Klose and Larsen in Ref. [23] and are not reproduced for brevity purposes.

$\alpha_1 = \frac{1}{2} + A_1$
$\alpha_2 = \frac{7}{24} + A_2$
$\beta_1 = 1 + B_1$
$\beta_2 = 1 + B_2$
$\gamma_1 = \frac{1}{8} + C_1$
$\gamma_2 = \frac{1}{8} + C_2$
$\delta_1 = D_1$
$\delta_2 = D_2$
$\nu_0 = \left[\frac{1}{4} + J_0 + \left(\frac{1}{2} + J_1\right)\xi_{11} + J_3\xi_{21}\right]$
$\nu_1 = \left[-\frac{3}{48} - \frac{2}{3}J_0 + \frac{1}{3}J_2 + \left(\frac{1}{2} + J_1\right)\xi_{12} + J_3\xi_{22}\right]$

$\xi_{11} = \frac{\alpha_1\beta_2 - 7\delta_1\gamma_2}{\beta_1\beta_2 - 21\delta_1\delta_2}$
$\xi_{12} = \frac{7\delta_1\alpha_2 - \gamma_1\beta_2}{\beta_1\beta_2 - 21\delta_1\delta_2}$
$\xi_{13} = \frac{\beta_2}{\beta_1\beta_2 - 21\delta_1\delta_2}$
$\xi_{14} = \frac{7\delta_1}{\beta_1\beta_2 - 21\delta_1\delta_2}$
$\xi_{21} = \frac{3\delta_2\xi_{11} - \gamma_2}{\beta_2}$
$\xi_{22} = \frac{3\delta_2\xi_{12} + \alpha_2}{\beta_2}$
$\xi_{23} = \frac{3\delta_2\xi_{13}}{\beta_2}$
$\xi_{24} = \frac{3\delta_2\xi_{14} + 1}{\beta_2}$

domain fluorescence molecular imaging where the SP_N model presented by Chu et al. was used [28].

We present a method for solving the forward and inverse problem for the FD-SPN model in (3)–(6). Altogether, we believe this work presents an attractive method for reconstructing the absorption and scattering coefficient of biological media from data obtained with the frequency modulated system. We focus on the model when $N = 3$, as this order ($N = 3$) has been shown to be accurate enough to capture transport behavior in tissue [23].

Our approach is based on the finite volume method (FVM) [13], which is distinct from all previous work that is based on either the finite difference method (FDM) [14,23] or the finite element method (FEM) [25,27,28]. The FVM allows for handling of complex geometry, which is a particularly important feature since DOT applications often involve complex geometries of arbitrary shape that can be most accurately modeled by unstructured grids. Furthermore, the FVM guarantees energy conservation, which is also very important when modeling the propagation of photon energy. The node-centered FV technique is particularly attractive for DOT because it provides computational efficiency in the forward problem, reducing the size of the resulting linear system. To be more specific, the standard FVM is based on the cell-centered discretization in which a control volume is a tetrahedral element itself. In contrast, the node-centered method constructs control volumes around the nodes of the tetrahedral mesh (also known as the "dual-mesh"). Typically, the node-centered method has much fewer control volumes than the cell-centered one; for example, the node-centered discretization of tetrahedral mesh yields one-seventh as many control volumes as does the cell-centered discretization, which leads to a great reduction in the size of the resulting linear system.

Therefore, we employ here a node-centered finite-volume method for discretization of the computational domain [29]. The resulting system of linear algebraic equations is solved with the restarted generalized minimal residual method (GMRES), which is a well-known Krylov subspace iterative method for solving systems of sparse linear equations [30]. The algorithm is implemented using objective-oriented programming in C++ for computational efficiency. The inverse problem is solved as a large-scale optimization problem. We address challenges of computing a Hessian matrix (H) or an approximate Hessian (B) through the use of a limited-memory Broyden-Fletcher-Goldfarb-Shanno (L-BFGS) algorithm [31]. Furthermore, with the L-BFGS algorithm we can avoid having to explicitly compute B; instead, only the product of B^{-1} and its associated vectors needs to be stored and updated for the calculation of the descent direction.

The forward and inverse algorithms are validated through numerical simulations. The algorithm for solving the forward problem is tested with numerical simulations on an inhomogeneous phantom. The SP_3 solutions are compared against the benchmark solutions based on the ERT model [13] in order to address computation time and accuracy. The performance of the proposed reconstruction algorithm is evaluated in terms of reconstruction accuracy and CPU times by using numerical phantoms.

The derivation of the finite volume approximation to the FD-SP_3 model is presented in Section 2. The algorithm for solving the inverse problem with the finite volume approximation to the FD-SP_3 model is presented in Section 3. Numerical phantoms for testing the forward and inverse models are presented in Section 4. Results for the forward and inverse problems are summarized in Section 5. This paper concludes with a discussion in Section 6.

2. Forward problem: finite-volume model

The FD-SP_3 model is defined by (3)–(6). In these equations, the outward pointing normal at the surface of the medium is denoted by $\hat{n}$ and S_1 and S_2 are the contributions of the boundary source, $S(\hat{\Omega})$, which are defined as

$$S_1 = \int_{\hat{\Omega}\cdot\hat{n}<0} S\left(\hat{\Omega}\right) 2\left|\hat{\Omega}\cdot\hat{n}\right| d\Omega, \tag{7}$$

$$S_2 = \int_{\hat{\Omega}\cdot\hat{n}<0} S\left(\hat{\Omega}\right)\left(5\left|\hat{\Omega}\cdot\hat{n}\right|^3 - 3\left|\hat{\Omega}\cdot\hat{n}\right|\right) d\Omega, \tag{8}$$

where $\hat{\Omega}$ denotes a discrete angular direction. The corresponding formula for the partial current is

$$J^+ = \left(\frac{1}{4} + J_0\right)\left(\phi_1 - \frac{2}{3}\phi_2\right) - D_1(0.5 + J_1)(\hat{n}\cdot\nabla\phi_1) + \left(\frac{5}{16} + J_2\right)\left(\frac{1}{3}\phi_2\right) - D_2(J_3)(\hat{n}\cdot\nabla\phi_2). \tag{9}$$

The coefficients J_n are defined in Appendix A.6 of [23] and not reproduced in this paper. To illustrate how the finite-volume versions of these equations are obtained, consider the discretization of domain O (Fig. 1a) with a triangular mesh (tetrahedral elements in 3D) (Fig. 1b). Control volume elements are defined around each node of the triangular mesh, resulting in either interior elements (Fig. 1b, element *a*) or boundary elements (Fig. 1b, element *b*). The outward pointing normal vector ($\hat{n}$) is now defined at each surface of the control volume elements (Fig. 1b). Consider an individual finite volume element $p \in V$ with S_I internal surfaces and S_B boundary surfaces (i.e. elements *a* or *b* in Fig. 1b). By definition, element p shares each of the surfaces S_I with a single neighboring control volume element. Let i denote the i-th neighbor of p, such that $i = 1 \ldots S_I$. Each surface of the control volume element has a corresponding normal vector $\hat{n}$.

Then, the finite volume version of the FD-SP_N model can be obtained by integrating (3)–(4) over each control volume of the dual mesh and then applying the Gauss divergence theorem to convert the volume integral into a surface integral along each surface of the control volume. The resulting surface integrals are computed using numerical quadrature rules, exploiting the fact that each volume element has a finite number of surfaces. The directional derivative terms that appear after application of the Gauss divergence theorem to (3)–(4) are simplified by using the two-node first-order differencing scheme based on two neighboring nodes, and are written in discretized form as follows,

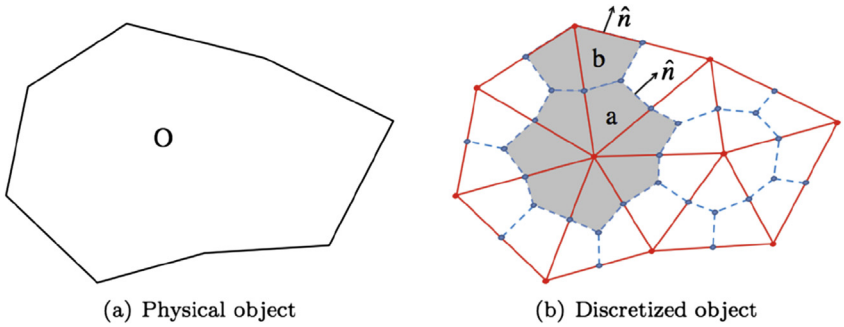

Fig. 1. (a) physical domain O; (b) discretization: triangular mesh (red) and dual mesh (blue). (For interpretation of the references to colour in this figure legend, the reader is referred to the web version of this article.)

$$\nabla\phi_1 \cdot \hat{n} \approx \frac{[\phi_1]_i - [\phi_1]_p}{dr_i}, \tag{10}$$

$$\nabla\phi_2 \cdot \hat{n} \approx \frac{[\phi_2]_i - [\phi_2]_p}{dr_i}, \tag{11}$$

where dr_i denotes the distance from the primary node p to its neighboring node i. With (10)–(11), the finite volume version of (3)–(4) (FV-FD-SP$_3$) is given by

$$-\sum_{i=1}^{S_I} D_1 \frac{[\phi_1]_i - [\phi_1]_p}{dr_i} dA_i + \left(\mu_a + \frac{i\omega}{v}\right)[\phi_1]_p \Delta V = [\dot{q}]_p \Delta V + \frac{2}{3}\left(\mu_a + \frac{i\omega}{v}\right)[\phi_2]_p \Delta V, \tag{12}$$

$$-\sum_{i=1}^{S_I} D_2 \frac{[\phi_2]_i - [\phi_2]_p}{dr_i} dA_i + \left(\frac{4}{9}\mu_a + \frac{5}{9}\mu_{a2} + \frac{1}{3}\frac{i\omega}{v}\right)[\phi_2]_p \Delta V = -\frac{2}{3}[\dot{q}]_m \Delta V + \frac{2}{3}\mu_a [\phi_1]_p \Delta V, \tag{13}$$

The corresponding discretized boundary equations are given by

$$\sum_{i=1}^{S_B} \xi_{11}[\phi_1]_p dA_i + \sum_{i=1}^{S_I} \xi_{12}[\phi_2]_p dA_i + \left(\mu_a + \frac{i\omega}{v}\right)[\phi_1]_p \Delta V - \frac{2}{3}\left(\mu_a + \frac{i\omega}{v}\right)[\phi_2]_p \Delta V = [\dot{q}]_p \Delta V + \sum_{i=1}^{S_B} \xi_{13}[S_1]_p dA_i + \sum_{i=1}^{S_B} \xi_{14}[S_2]_p dA_i, \tag{14}$$

$$\sum_{i=1}^{S_B} \xi_{21}[\phi_1]_p dA_i + \sum_{i=1}^{S_B} \xi_{22}[\phi_2]_p dA_i + \left(\frac{4}{9}\mu_a + \frac{5}{9}\mu_{a2} + \frac{1}{3}\frac{i\omega}{v}\right)[\phi_2]_p \Delta V - \frac{2}{3}\mu_a [\phi_1]_p \Delta V = -\frac{2}{3}[\dot{q}]_p \Delta V + \sum_{i=1}^{S_B} \xi_{13}[S_1]_p dA_i + \sum_{i=1}^{S_B} \xi_{14}[S_2]_p dA_i. \tag{15}$$

Finally, the discretized partial current operator of equation (9) is given by

$$\left[J^+\right]_p = \nu_0 [\phi_1]_p + \nu_1 [\phi_2]_p, \tag{16}$$

where coefficients ξ_{ij} and ν_n are defined in Table 1. These coefficients are functions of boundary coefficients A_n, B_n, C_n, and D_n, which are themselves functions of the various angular moments of the reflectivity R. The definitions of these boundary coefficients are given in Appendix A.2 of [23].

Equations (12–15) can be rewritten to form a system of linear equations, $Au = b$, where $A \in C_{2M} \times C_{2M}$ is the discretized SP$_3$ model, $u = [\phi_1^T\ \phi_2^T]^T \in C_{2M}$ is the composite moments of the fluence, and $b \in R_{2M}$ is the source vector that accounts for boundary or/and interior light sources. The partial current, $J^+(r)$, is formally computed as

$$J^+(r, \omega) = Qu, \tag{17}$$

where $Q \in R_{N \times 2M}$ is a projection operator that transforms the composite moments of the fluence u into the partial currents. Here, N is the total number of source-detector pairs. This system of equations is solved using the restarted GMRES algorithm [30,32].

For improved computational performance, it is helpful to rewrite the final discretized form of the SP$_3$ model defined by (12)–(15). The absorption and scattering coefficients are inherently in significantly different scales ($\mu_s \gg \mu_a$), which can lead to slow convergence during the reconstruction process. This issue can be overcome by defining scaled absorption coefficient $\widehat{\mu_a} = l_a \mu_a + c_a$ and scaled scattering coefficient $\widehat{\mu_s} = l_s \mu_s + c_s$, where constants l_a, c_a, l_s, and c_s are computed so that $\widehat{\mu_a} \in [-1, 1]$ and $\widehat{\mu_s} \in [-1, 1]$ relative to the predefined lower and upper limits for μ_a and μ_s, for example, $\mu_a \in [0.0,\ 1.0] cm^{-1}$, and $\mu_s \in [0.0,\ 200.0] cm^{-1}$, assuming the anisotropic factor $g \approx 0.9$. We note that these upper and lower bounds are for rescaling purposes only and should not be confused with constraints on the admissible values of the variables.

The diffusion operator (D_1, D_2) appearing in (12)–(13) are defined at the surface of the control volume; therefore, it must be given as a function of nodal values. This is achieved by replacing the D_1 and D_2 with their average value between node p and its neighboring node i, given by $D_1 = 0.5 \times ([D_1]_p + [D_1]_i)$, $D_2 = 0.5 \times ([D_2]_p + [D_2]_i)$, respectively. Thus, the final version of the SP$_3$ model can be obtained by expanding D_1 and D_2, expanding all $\mu_{a,n}$ terms, and then replacing μ_a and μ_s with $\widehat{\mu_a}$ and $\widehat{\mu_s}$ throughout.

Algorithm 1. Gradient of SP_3 model matrix A with respect to μ_s

$\nabla_{\mu_s} A \leftarrow 0$
for$(i = 0; i < M; i++)$ **do**
  $\nabla_{\mu_s} A_{ii} += \Delta V_i$
  for$(j = 0; j < S_T; j++)$ **do**
    if$(S_j$ is interior surface$)$ **then**
      $k \leftarrow$ neigbor node number
      $\beta_1 \leftarrow \beta_1 - \frac{3(1-g)}{2l_s}\left[\frac{dA_j}{dr_j}\right][D_1]_i^2$
      $\beta_2 \leftarrow \beta_2 - \frac{7(1-g^3)}{2l_s}\left[\frac{dA_j}{dr_j}\right][D_2]_i^2$
      $\nabla_{\mu_s} A_{iik} \leftarrow -\frac{3(1-g)}{2l_s}\left[\frac{dA_j}{dr_j}\right][D_1]_i^2$
      $\nabla_{\mu_s} A_{iki} \leftarrow \frac{3(1-g)}{2l_s}\left[\frac{dA_j}{dr_j}\right][D_1]_i^2$
      $\nabla_{\mu_s} A_{ikk} \leftarrow \frac{3(1-g)}{2l_s}\left[\frac{dA_j}{dr_j}\right][D_1]_i^2$
      $\nabla_{\mu_s} A_{i+M,i+M,k} \leftarrow -\frac{7(1-g^3)}{2l_s}\left[\frac{dA_j}{dr_j}\right][D_2]_i^2$
      $\nabla_{\mu_s} A_{i+M,k+M,i} \leftarrow \frac{7(1-g^3)}{2l_s}\left[\frac{dA_j}{dr_j}\right][D_2]_i^2$
      $\nabla_{\mu_s} A_{i+M,k+M,k} \leftarrow \frac{7(1-g^3)}{2l_s}\left[\frac{dA_j}{dr_j}\right][D_2]_i^2$
    end if
  end for
$\nabla_{\mu_s} A_{iii} \leftarrow \beta_1$
$\nabla_{\mu_s} A_{i+M,i+M,i} \leftarrow \frac{5(1-g^2)}{9l_s}[\Delta V]_i + \beta_2$
end for

Algorithm 2. Gradient of SP_3 model matrix A with respect to μ_a

$\nabla_{\mu_a} A \leftarrow 0$
for$(i = 0; i < M; i++)$ **do**
  $\nabla_{\mu_a} A_{ii} += \Delta V_i$
  for$(j = 0; j < S_T; j++)$ **do**
    if$(S_j$ is interior surface$)$ **then**
      $k \leftarrow$ neigbor node number
      $\beta_1 \leftarrow \beta_1 - \frac{3}{2l_a}\left[\frac{dA_j}{dr_j}\right][D_1]_i^2$
      $\beta_2 \leftarrow \beta_2 - \frac{7}{2l_a}\left[\frac{dA_j}{dr_j}\right][D_2]_i^2$
      $\nabla_{\mu_a} A_{iik} \leftarrow -\frac{3}{2l_a}\left[\frac{dA_j}{dr_j}\right][D_1]_i^2$
      $\nabla_{\mu_a} A_{iki} \leftarrow \frac{3}{2l_a}\left[\frac{dA_j}{dr_j}\right][D_1]_i^2$
      $\nabla_{\mu_a} A_{ikk} \leftarrow \frac{3}{2l_a}\left[\frac{dA_j}{dr_j}\right][D_1]_i^2$
      $\nabla_{\mu_a} A_{i+M,i+M,k} \leftarrow -\frac{7}{2l_a}\left[\frac{dA_j}{dr_j}\right][D_2]_i^2$
      $\nabla_{\mu_a} A_{i+M,k+M,i} \leftarrow \frac{7}{2l_a}\left[\frac{dA_j}{dr_j}\right][D_2]_i^2$
      $\nabla_{\mu_a} A_{i+M,k+M,k} \leftarrow \frac{7}{2l_a}\left[\frac{dA_j}{dr_j}\right][D_2]_i^2$
    end if
  end for
$\nabla_{\mu_a} A_{iii} \leftarrow \frac{[\Delta V]_i}{l_a} + \beta_1$
$\nabla_{\mu_a} A_{i+M,i+M,i} \leftarrow -\frac{2}{3}\frac{[\Delta V]_i}{l_a}$
$\nabla_{\mu_a} A_{i+M,i+M,i} \leftarrow -\frac{2}{3}\frac{[\Delta V]_i}{l_a}$
$\nabla_{\mu_a} A_{i+M,i+M,i} \leftarrow \frac{[\Delta V]_i}{l_a} + \beta_2$
end for

3. Inverse problem: reconstruction algorithm

With the SP_3 equation used as a forward model, the resulting inverse problem can be written in general terms as follows:

$$\min f(x,u) = \frac{1}{2}(P-M)^T\left(\overline{P-M}\right) + \beta R(x) \text{ subject to } c(x,u) = A(x)u - b = 0. \tag{18}$$

where x denote inverse variables (i.e., $x \in [\mu_a, \mu_s]$), u denotes the fluence vector, $P(=Qu)$ and M are predictions and measurements of partial currents J^+ ; $f(x,u)$ is an objective function that quantifies the least square error between predictions P and measurements M; the operator $\overline{(\cdot)}$ is the complex conjugate of the complex-valued term; $R(x)$ denotes appropriate regularization with a regularization parameter β; $Au = b$ (or $c = 0$) denotes a discretized forward equation. Note that we use in this work *Alifanov's iterative regularization methods* [34] as an alterative to Tikhonov-type regularization methods.

The solution of the inverse problem given by (18) can be found by iteratively minimizing the objective function $f(x,u)$ with respect to the inverse variable x. Newton methods solve problem (18) by minimizing a quadratic approximation of the objective function $f(x,u)$ as follows:

$$\min \Delta x^T \nabla_x f + \frac{1}{2}\Delta x^T H_{xx} \Delta x \tag{19}$$

where Δx is the update of inverse variable, and $\nabla_x f$ and H_{xx} are the gradient vector and Hessian matrix of the objective function f with respect to the inverse variable x. Minimization of (19) with respect to Δx gives the following form of the update Δx of inverse variable x:

$$\Delta x = H_{xx}^{-1} \nabla_x f. \tag{20}$$

Here direct computation of the Hessian matrix inversion H_{xx}^{-1} is avoided and instead we directly approximate the matrix-vector product $H_{xx}^{-1}\nabla_x f$ by using the L-BFGS method reported in DOT literature [13,33,35]. The gradient calculation $\nabla_x f$ required by the L-BFGS method is computed by following the adjoint method reported in Ref. [13] as:

$$\nabla_x f = \left(u^T \frac{\partial A^T}{\partial x} \lambda \right)_{Re}, \tag{21}$$

where $(\cdot)_{Re}$ denotes the real-valued part of the complex-valued term $(\cdot)$ and the adjoint variable, $\lambda \in C_{2M}$, can be computed by solving the following adjoint equation,

$$A^T \lambda = -\left[Q^T \left(\overline{Qu - M} \right) \right], \tag{22}$$

where the linear problem (22) is solved using the restarted GMRES algorithm as described above. Note that we use in practice the rescaled gradient defined as the gradient (21) divided by each cell volume, multiplied by the average cell volume, which is to reduce grid effects due to inhomogeneous cell sizes on unstructured meshes.

As can be seen in equation (21), the gradient $\nabla_x f$ requires the calculation of the gradient of the discretized FV-FD-SP_3 matrix, $\partial A^T / \partial x$. In this work, we perform exact differentiation of the discretized FV-FD-SP_3 matrix A with respect to μ_a and μ_s respectively. The formulae for computing this term depend on the order of the SP_N model. Algorithms 1 and 2 present the definitions of the partial derivatives of A with respect to μ_s and μ_a for $N = 3$, respectively.

To ensure global convergence of the L-BFGS method, a cubic interpolation line search is performed here to find a step length α that provides a sufficient decrease in the objective function f [35]. As a consequence, the new iterate is given by

$$x^{k+1} = x^k + \alpha \Delta x^k. \tag{23}$$

All terms are now well defined to perform reconstructions with the FV-FD-SP_3 model and the L-BFGS algorithm can be applied directly. Derivation of the FV-FD-SP_1 (and indeed for $N = 5$ or 7) can be performed by following similar steps to those given in (19)–(23).

4. Numerical phantoms

4.1. Forward problem

The fluence ψ and partial current J^+ solutions obtained with the FV-FD-SP_N model are compared to those with a benchmark algorithm based on the ERT model using a dense set of discrete ordinates (S_{12}). We use a circular phantom with a diameter of 2.0 cm whose origin is at the center of the disk ($x = 0.0\ cm, y = 0.0\ cm$). The performances of the FV-FD-SP_N model are analyzed using an inhomogeneous medium with high-absorbing or/and low-scattering inclusions. Together, these phantoms provide insight into the validity of various SP_N models in the non-diffuse regime.

The numerical phantom is discretized with a dense mesh to ensure that the numerical error from the ERT discretization is minimal. The mesh consists of 37,247 mesh nodes and 73,236 triangular elements, resulting in an FVM mesh with 37,247 control volume elements and 220,964 surfaces. The FEM and FVM grids are not shown here since they are too dense to display. Instead, the significantly less dense FEM and FVM meshes of the same phantom are shown for illustration (Fig. 2a,b). The computation time required to generate the FVM mesh from the FEM mesh is minimal (0.05s for this phantom) and generally ignored.

There is a source on the boundary of the disk (at position $x = 0.7071\ cm,\ y = 0.7071\ cm$) with source power $S(\widehat{\Omega}) = 1.0\ Wcm^{-2}sr^{-1}$ and 50 detectors distributed evenly around the phantom boundary at points away from the source (Fig. 2c). Equations (12–15) are solved for ϕ_1 and ϕ_2 on all 37,247 FVM elements, which are then used to compute the partial current at each detector position using (16).

The optical properties of the phantoms are summarized in Table 2 and the specific location of the inclusions and their optical properties are shown in Fig. 3. The first phantom is homogeneous with low absorption ($\mu_a = 0.001 cm^{-1}$) and high scattering ($\mu_s = 400 cm^{-1}, g = 0.95$). This medium simulates highly diffuse tissue where the diffusion equation is known to be an accurate model of light propagation.

The second phantom contains high-absorbing inclusions and low-scattering inclusions (Fig. 3), where each of the inclusions is a disk with 0.25 cm diameter. The second phantom is designed to test the accuracy of the SP_3 model in the transport regime, where the diffusion equation is known to be a poor approximation to the ERT.

The relative error $J_e^+(r)$ between the benchmark partial current $J_{ERT}^+(r)$ computed with ERT (S_{12}) and the partial current $J_{SP3}^+(r)$ with the FV-FD-SP3 is computed at each node i using the following formula:

$$J_e^+(r)_i = 100 \times \frac{J_{SP3}^+(r)_i - J_{ERT}^+(r)_i}{J_{ERT}^+(r)_i}. \tag{24}$$

The average relative error $\widetilde{J_e}(r)$ of the partial current is also reported as a measure of overall error. The relative error $\psi_e(r)$ between the benchmark fluence $\psi_{ERT}(r)$, and the zeroth order moment $\psi_{SP3}(r)$ of the SP_3 model (i.e., $\psi_0 = \phi_1 - 2\phi_2$) is computed at each node i using (24). A second parameter that quantifies the error between the SP_3 and ERT solutions is the volume-averaged error $\tilde{\psi}_e$ over the entire computational domain as given by (25).

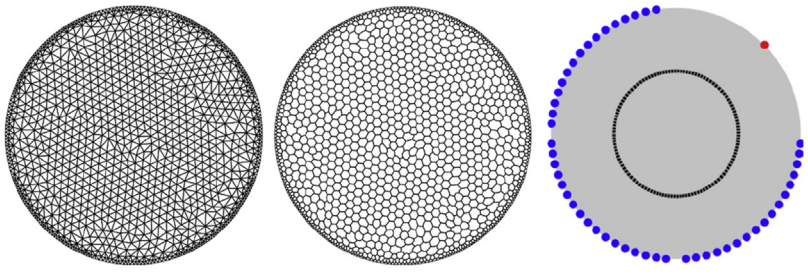

(a) FEM mesh (b) FVM mesh (c) Source and detectors

Fig. 2. Discretization of a disk (2.0 cm diameter) into (a) triangular elements (i.e. FEM mesh) and (b) into finite-volume elements (i.e. FVM mesh). (c) A single boundary source (red dot) and 50 detectors (blue dots) are distributed around the boundary of the phantom. The internal cross-section of interest consists of mesh points 0.5 ± 0.01 cm from the center of the phantom, represented by the inner circle. (For interpretation of the references to colour in this figure legend, the reader is referred to the web version of this article.)

Table 2
Optical properties of the 2D inhomogeneous phantoms used for the forward simulations. Subscripts 'b' and 'o' denote the optical properties of the background and the inclusion objects, respectively.

#	$\mu_{a,b}[cm^{-1}]$	$\mu_{s,b}[cm^{-1}]$	$\mu_{a,o}[cm^{-1}]$	$\mu_{s,o}[cm^{-1}]$	g	n_m	ω [MHz]
1	0.1	200.0	0.5	100	0.95	1.4	600
2	0.1	100.0	1.0, 2.0	–	0.95	1.4	600
3	0.1	200.0	–	20, 60	0.95	1.4	600

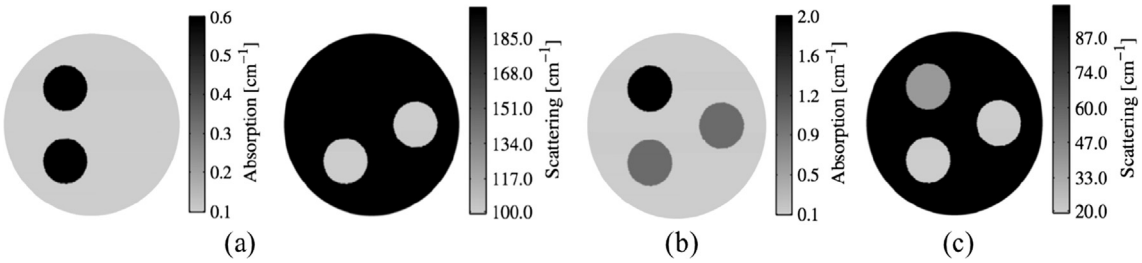

Fig. 3. Definition of two-dimensional inhomogeneous phantoms; (a) Phantom #1; (b) Phantom #2; (c) Phantom #3.

$$\psi_e(r)_i = 100 \times \frac{\psi_{SP3}(r)_i - \psi_{ERT}(r)_i}{\psi_{ERT}(r)_i}\ , \quad \tilde{\psi}_e = \frac{100}{V} \times \sum_{i=1}^{N} \left(\frac{\psi_{SP3}(r)_i - \psi_{ERT}(r)_i}{\psi_{ERT}(r)_i} \right) \Delta V_i \tag{25}$$

where V represents the total computational volume and ΔV the control volume of each FVM element. The GMRES algorithm is set to restart after 30 iterations with no limit on the number of total iterations. The convergence criterion is set to 1.0×10^{-12}. All computations are performed on a 2.4 GHz Mac Pro.

4.2. Inverse problem

We evaluate the performance of the SP_3-based reconstruction algorithm through numerical simulations on a 2D circular phantom and a 3D finger phantom as defined in Fig. 4 and Table 3. Absorbing and scattering inclusions are placed inside each phantom and simulated measurement data (M) is generated using the ERT on a dense FVM mesh and corrupted with 1.0% Gaussian noise, whereas reconstructions are performed on a coarser mesh to mitigate the risk of committing a so-called '*inverse crime*' during the reconstruction process. All simulations on these phantoms are performed with $g = 0.95$, $\omega = 600\,MHz$, and $n_m = 1.4$ as typically encountered in real-world applications, and also started with a homogeneous initial guess for μ_a and μ_s'. The 2D phantom is defined to have 8 boundary sources and 68 detectors distributed along the perimeter of a circle with a diameter of 2 *cm* (Fig. 4a and b). The 3D finger phantom from the 3D scan of actual human finger is selected here since we are interested in applying FD-DOT to the imaging of finger joints [17–22]. In total, 11 distinct point sources (Fig. 4c) and 155 detector points (Fig. 4d) are defined on this phantom surface, and with this trans-illumination setup the finger is illuminated on the posterior (dorsal) side and escaping photons are measured on the anterior (palmar) side [17].

Table 3
Parameters used in different reconstruction cases.

	2D phantom	3D phantom
Geometry	disk	finger
Background absorption [cm^{-1}]	0.1	0.1
Inclusion absorption [cm^{-1}]	0.2	0.25
Background reduced scattering [cm^{-1}]	10.0	12.5
Inclusion reduced scattering [cm^{-1}]	6.0	7.5
Number of sources	8	11
Number of detectors	68	552

The accuracy of each reconstruction is quantified using the correlation coefficient $\rho \in [-1, 1]$ and the deviation factor $\delta \in [0, \infty)$ defined as

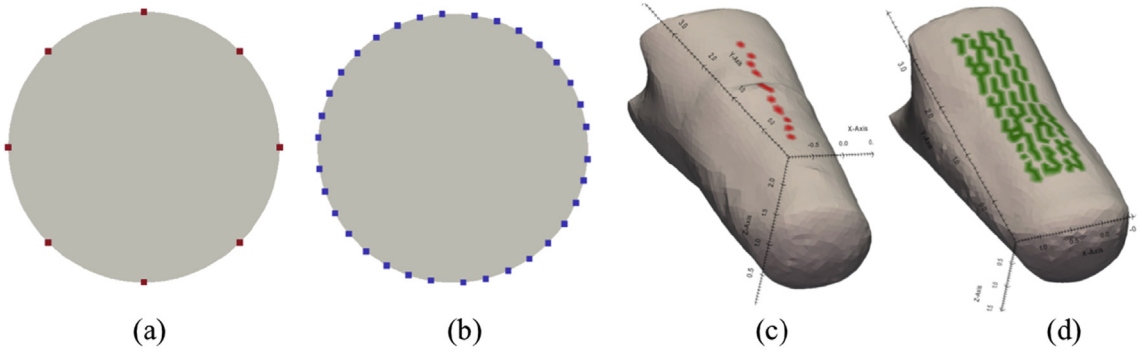

Fig. 4. Geometries and source-detector configuration of test phantoms: (a) sources and (b) detectors for the 2D phantom; (c) sources on the posterior and (d) detectors on the anterior surface for the finger-like phantom.

$$\rho = \frac{\sum_{i=1}^{n}\left(\mu_i^r - \overline{\mu^r}\right)\left(\mu_i^a - \overline{\mu^a}\right)}{(n-1)\sigma(\mu^r)\cdot\sigma(\mu^a)}, \quad \delta = \frac{\sqrt{\sum_{i=1}^{n}\left(\mu_i^a - \mu_i^r\right)^2/n}}{\sigma(\mu^a)} \tag{26}$$

where μ^a is the analytic (i.e., exact) solution, μ^r is the reconstruction image, $\overline{\mu^a}$ and $\overline{\mu^r}$ are the mean values and $\sigma(\mu^a)$ and $\sigma(\mu^r)$ are the standard deviations of μ^a and μ^r respectively, and n refers to the total number of distinct mesh nodes. The correlation coefficient ρ is between -1 and 1, with $\rho = 1.0$ corresponding to an exact match between the analytical and reconstruction images. The deviation factor $\delta \in [0, \infty)$ denotes normalized root mean square error. Accordingly, the closer ρ gets to 1 and δ to 0, the better is quality of reconstruction. The reconstruction is terminated when the objective function value decreases by four orders of magnitude from its original value and the relative change rate in the objective function is as small as 1×10^{-6}.

5. Results

5.1. Forward problem

Results from simulations on an inhomogeneous phantom defined in Table 2 and Fig. 3, are summarized in this section. Images of the amplitude and the phase of the fluence are presented in Figs. 5 and 6, respectively, for the first phantom (Phantom #1). Plots of the partial current at boundary detectors are presented in Fig. 7. The individual composite moments of the SP_3 model are shown in Fig. 8.

The amplitude and phase components of the fluence computed with the FD-SP_3 and the FD-ERT (S_{12}) are shown in Fig. 5(a and b) and 6 (a,b), respectively. The errors of the FD-SP_3 relative to the FD-ERT (S_{12}) at mesh nodes are shown in Figs. 5c and 6c. With SP_3 the average relative errors $\widetilde{\psi_e}(r) = 6.01\%$, $\widetilde{J_e^+}(r) = 7.1\%$ for the amplitude, and $\widetilde{\psi_e}(r) = 3.28\%$ and $\widetilde{J_e^+}(r) = 3.67\%$ for phase, respectively, whereas for SP_1 errors $\widetilde{\psi_e}(r) = 6.40\%$, $\widetilde{J_e^+}(r) = 8.21\%$ for amplitude and errors $\widetilde{\psi_e}(r) = 3.13\%$, $\widetilde{J_e^+}(r) = 3.80\%$ for phase. These differences are within the range reported in Ref. [23].

In general, the error within the medium is relatively small and substantial errors only occur near the location of the source in both amplitude and phase, which likely corresponds to regions of the medium where significant transport behavior occurs and where the SP_3 model cannot directly account for such behavior. These observations are also pronounced in the partial current (Fig. 7).

Fig. 8 shows the first and second composite moments of the fluence, ϕ_1 and ϕ_2, respectively. Recalling that the zeroth order Legendre moment of the fluence is defined as $\psi_0 = \phi_1 - 2\phi_2$, then we can think of the first composite moment, ϕ_1, as equivalent to the solution obtained with the diffusion equation (i.e. when $N = 1$). The second composite moment, ϕ_2, is then a term that effectively corrects the diffusion solution ϕ_1, taking into account the 'transport' behavior of photons over the entire domain. Fig. 8a,b clearly shows this: there is a strong "correction" near the source and within the three disks where photons exhibit more 'transport-like' behaviors. Note that photons do not experience much scattering near the source and also the scattering coefficients of the three disks are lower than the background. Likewise, the phase component of ϕ_2 also corrects the phase component ϕ_1 near the source. In regards to computational requirements, the benefit of using the FD-SP_3 model over the ERT (S_{12}) model is clear. The FD-SP_3 model took 113 s and 313 Mbytes and the FD-SP_1 model 70 s and 176 Mbytes whereas the benchmark ERT (S_{12}) model took 6715 s and over 6.1 Gbytes to converge. The difference in speed is approximately 60× and the reduction in RAM is over 19×.

The second phantom is considered here that contains extremely high absorbing inclusions ($\mu_a = 1.0 \sim 2.0\ cm^{-1}$). Fig. 9 shows the results of the SP_3 model for the second phantom (Phantom #2) in terms of ϕ_1 and ϕ_2 of amplitude and phase. For the average relative errors, the SP_3 gives $\widetilde{\psi_e}(r) = 5.47\%$, $\widetilde{J_e^+}(r) = 11.82\%$ for the amplitude, and $\widetilde{\psi_e}(r) = 2.54\%$ and $\widetilde{J_e^+}(r) = 1.52\%$ for phase, respectively whereas the SP_1 yields $\widetilde{\psi_e}(r) = 8.51\%$, $\widetilde{J_e^+}(r) = 15.21\%$ for amplitude and

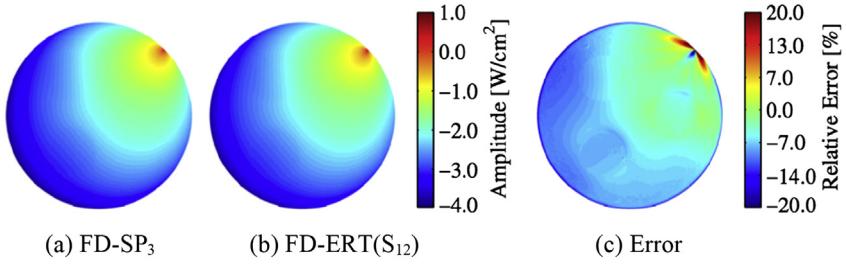

Fig. 5. Phantom #1: amplitude (log scale) component of the fluence computed with the (a) FD-SP_3 and (b) FD-ERT (S_{12}) models; (c) percent error in the amplitude component of the FD-SP_3 relative to the FD-ERT (S_{12}) model.

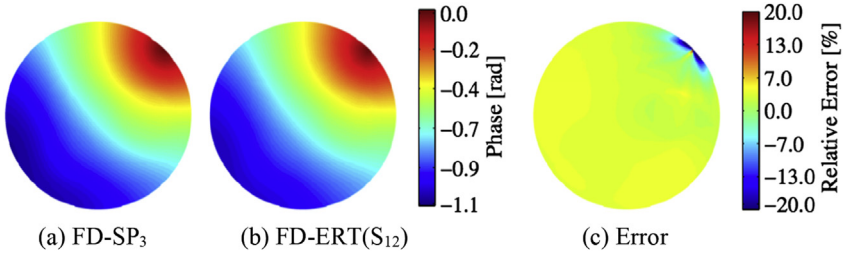

Fig. 6. Phantom #1: phase component of the fluence computed with the (a) SP_3 and (b) ERT (S_{12}) models; (c) percent error in the phase component of the FD-SP_3 relative to the FD-ERT (S_{12}) model.

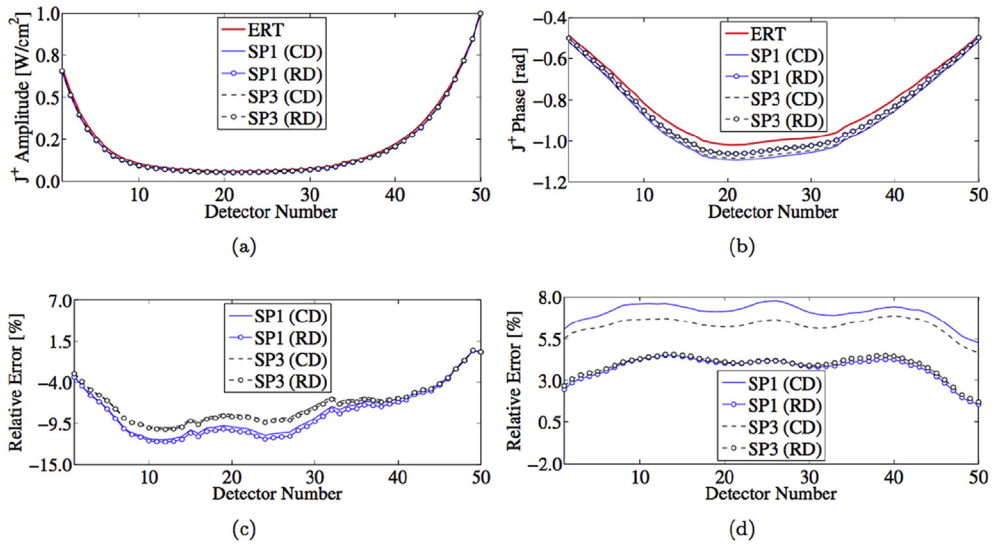

Fig. 7. Phantom #1: (a,b) amplitude and phase of the partial current, J^+ and (c,d) Error in the amplitude and the phase of the partial current, J_e^+. Detectors are numbered sequentially: 1 and 50 (nearest to source) and 25 (most distant from source).

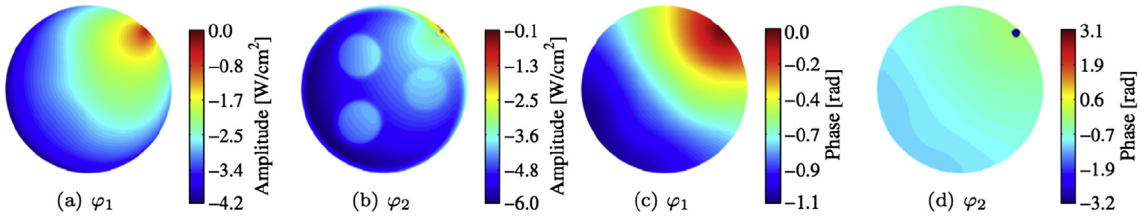

Fig. 8. Phantom #1: (a, b) Amplitude component (log scale) and (c, d) phase component of ϕ_1 and ϕ_2, computed with the FD-SP_3 model.

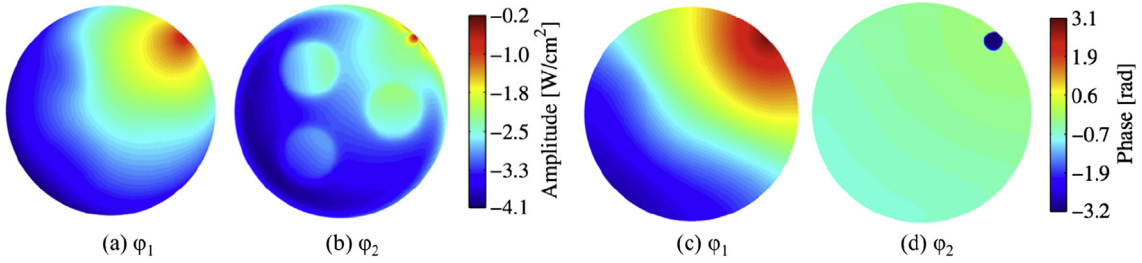

Fig. 9. Phantom #2: (a, b) Amplitude component (log scale) and (c, d) phase component of ϕ_1 and ϕ_2, computed with the FD-SP_3 model.

$\widetilde{\psi_e}(r) = 5.44\%$, $\widetilde{J_e^+}(r) = 8.68\%$ for phase. Overall, the errors are larger in both amplitude and phase and the differences between the SP_1 and SP_3 solutions are also more pronounced here, i.e., the error values here indicate that the SP_3 solutions are almost 100% more accurate than the SP_1 solutions in this case where very high absorbing inclusions are considered. Computational times are almost half of those with the first phantom as the SP_3 took 63 s and the SP_1 30 s, and the ERT (S_{12}) 4819 s. This reduction is expected since the larger absorption coefficient makes the diagonal terms larger in the linear system $Au = b$ and as a consequence leads to faster convergence.

Lastly, we present the results of the third phantom with highly lower scattering inclusions relative to the background. Fig. 10 shows the distributions of ϕ_1 and ϕ_2 for amplitude and phase. The scattering inclusions are identifiable in the ϕ_2 image of amplitude (Fig. 10b) but not in the ϕ_2 image of phase (Fig. 10d). Also the contrast at the site of the scattering inclusions is lower than the contrast at the site of the absorbing inclusions considered in the second phantom, particularly in the amplitude images (Fig. 9b vs. Fig. 10b). The relative errors for the fluence distribution and the partial currents are calculated as the SP_3 gives $\widetilde{\psi_e}(r) = 4.69\%$, $\widetilde{J_e^+}(r) = 12.88\%$ for the amplitude, and $\widetilde{\psi_e}(r) = 3.94\%$ and $\widetilde{J_e^+}(r) = 3.04\%$ for phase, respectively whereas the SP_1 yields $\widetilde{\psi_e}(r) = 4.99\%$, $\widetilde{J_e^+}(r) = 13.79\%$ for amplitude and $\widetilde{\psi_e}(r) = 3.56\%$, $\widetilde{J_e^+}(r) = 5.00\%$ for phase. Overall the SP_3 model performs better than the SP_1 model in the calculations of both fuence and phase. The computation times required to obtain the solutions with the models are 205 s (SP_3), 99 s (SP_1), and 7816 s (S_{12}), which are larger than when only highly absorbing inclusions are considered.

5.2. Inverse problem

The optical properties of the 2D circular phantom used to

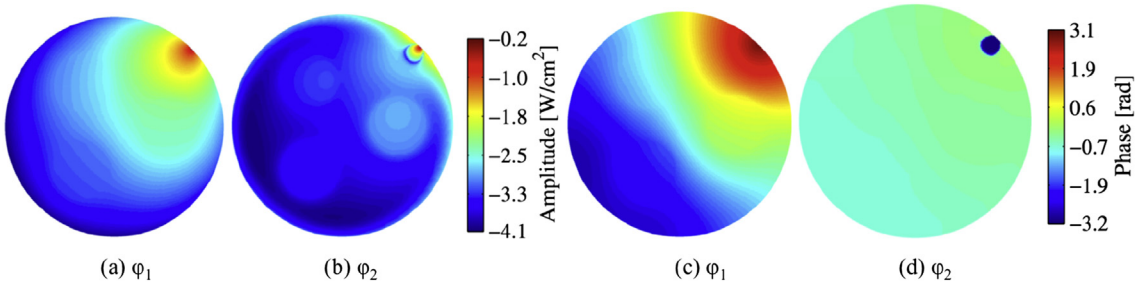

Fig. 10. Phantom #3: (a, b) Amplitude component (log scale) and (c, d) phase component of ϕ_1 and ϕ_2, computed with the FD-SP$_3$ model.

evaluate the performance of the SP$_3$-based reconstruction algorithm are chosen to be outside the diffuse regime, with two inclusions of higher absorption and two additional inclusions of lower scattering in a moderately diffuse background as shown in Fig. 11a,c. Overall, both SP$_1$ and SP$_3$ reconstructions identify the inclusions well (based on separation). In terms of quantified accuracy, however, the SP$_3$ model gives more accurate reconstructions (i.e., higher correlation and less deviation) than the SP$_1$ model: the correlation coefficient and the deviation factor of the SP$_3$ model are $\rho(\mu_a) = 0.82$, $\delta(\mu_a) = 0.58$ and $\rho(\mu_s') = 0.86$, $\delta(\mu_s') = 0.53$ whereas for the SP$_1$ model $\rho(\mu_a) = 0.76$, $\delta(\mu_a) = 0.68$ and $\rho(\mu_s') = 0.73$, $\delta(\mu_s') = 0.84$. Computationally, the SP$_3$ model exhibits faster decay rate in the inverse error compared to the SP$_1$ model as clearly shown in Fig. 12a. The faster decay rate by the SP$_3$ can be understood from the fact that the SP$_3$ model provides more accurate predictions of partial currents than the SP$_1$ model and as a result the SP$_3$ model decreases the inverse error at a faster rate than the SP$_1$. In terms of CPU times, the SP$_3$ reconstruction takes approximately 73.0% more time than the SP$_1$ reconstruction for the objective function value to decrease to 1×10^{-3} (Fig. 12b). This is expected as the SP$_3$ model has twice as many forward variables as the SP$_1$ model while the number of inverse variables remains the same for both models. It should be however noted that the SP$_1$

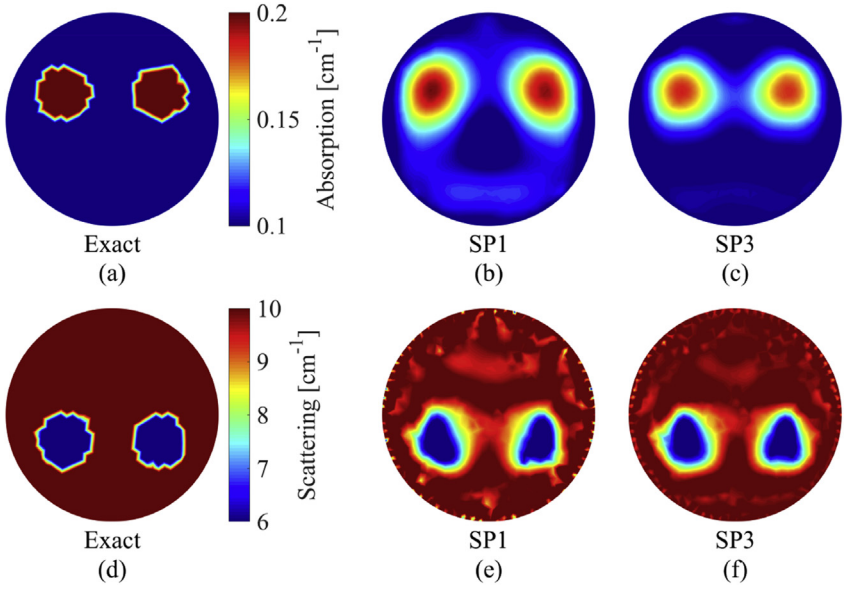

Fig. 11. Reconstruction images of μ_a (top) and μ_s' (bottom) of the 2D circular phantom: (a,d) exact; (b,e) SP$_1$ reconstructions; (c,f) SP$_3$ reconstructions.

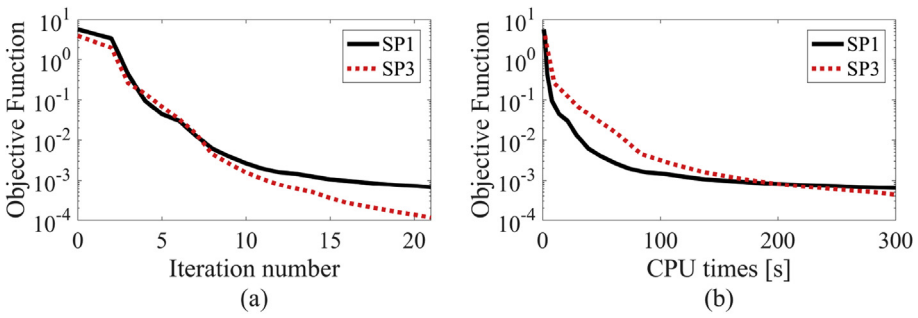

Fig. 12. Convergence of the reconstruction algorithms with respect to (a) time and (b) iteration number.

reconstruction model slows down quickly as it attempts to further minimize the inverse error below 1×10^{-3}. This type of degradation in convergence is due to the fact that the SP_1 model is less accurate than the SP_3 model in predicting partial currents in non-diffuse regime as described earlier.

We also investigate effects of using the different numbers of sources and detectors on reconstruction quality. For this study, the same 2D circular phantom as before is considered here. But this time we change the numbers of sources and detectors in two different pairs: one pair of 4 source and 68 detectors and another pair of 8 sources and 34 detectors. The reconstructions are performed with these two source-detector pairs and the correlation coefficient and the deviation factor are calculated to evaluate image quality for each case. The results are given in Figs. 13 and 14 and in Table 4, respectively. As shown in Fig. 13, the reconstructions with 8 sources and 34 detectors do not resolve the absorption inclusions well, only leading to one big continuous blob, whereas the reconstructions with 4 sources and 68 detectors produce spatially well-resolved results of both absorption and scattering coefficients. In terms of quantitative image quality, it is remarkable that the data of 4 sources and 68 detectors achieves similar accuracy to the full set of 8 sources and 68 detectors as clearly seen in Table 4 and Fig. 14. It appears from these results that the number of detectors has more significant impact on the reconstruction quality than the number of sources does. In other words, these results imply that increasing the number of detectors can have more advantage over increasing the number of sources, which also means that the use of fewer sources and more detectors is computationally more efficient than the use of more sources and fewer detectors when the same amount of measurement data is required. Computationally, the SP_1 and SP_3 algorithms show similar behaviors as shown in Fig. 12 for these two cases both with respect to CPU times and convergence, although not presented here.

Finally we present here the reconstruction results of the 3D finger phantom as shown in Fig. 4 (c,d). The dimension of the finger under consideration is approximately 4.0 cm in length (y-axis) and has width and height of approximately 2.0 cm. As shown in Fig. 15, the phantom has one inclusion of elevated absorbing and one

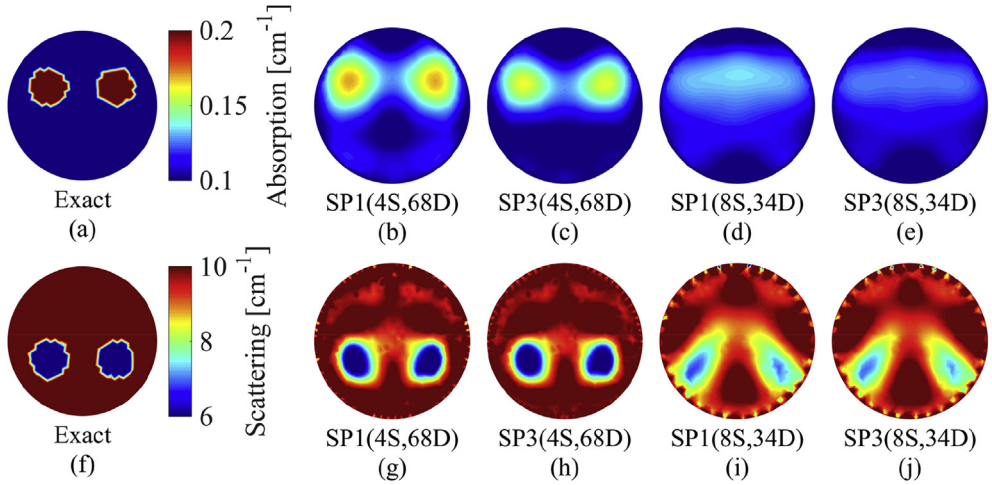

Fig. 13. Reconstruction images of μ_a (top) and μ_s' (bottom) obtained using the different numbers of sources and detectors: (a,f) exact; (b,c,g,h) 4 sources and 68 detectors; (d,e,i,j) 8 sources and 34 detectors with SP_1 and SP_3 reconstructions.

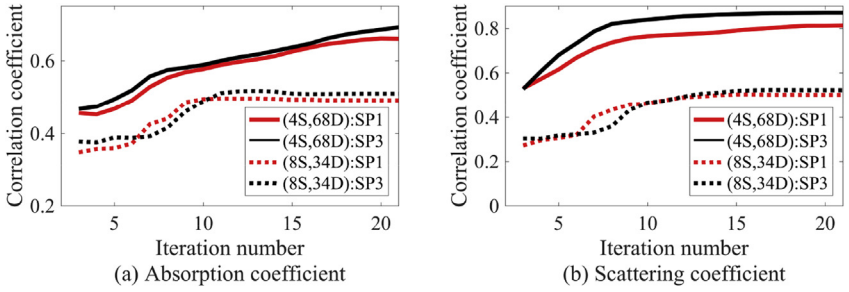

Fig. 14. Correlation coefficients of μ_a (left) and μ_s' (right) obtained with the two reconstruction methods using different numbers of sources and detectors during the iterative reconstruction process.

Table 4
Correlation coefficients and deviation factors between reconstructed and exact optical map as shown in Fig. 13.

Sources and detectors used	Methods	Cor. $\rho(\mu_a)$	Dev. $\delta(\mu_a)$	Cor. $\rho(\mu_s')$	Dev. $\delta(\mu_s')$
(4 sources, 68 detectors)	SP_1	0.67	0.77	0.82	0.62
	SP_3	0.72	0.71	0.86	0.51
(8 sources, 34 detectors)	SP_1	0.49	0.88	0.50	0.98
	SP_3	0.51	0.87	0.52	0.91

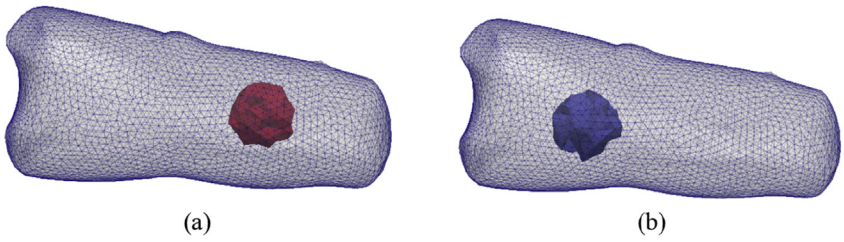

Fig. 15. Sagittal views of the finger phantom with one elevated absorbing (a) and one lower scattering (b) inclusion in a homogeneous background, and their optical properties are given in Table 3.

inclusion of lower scattering as compared to the background. The inclusions are spheres with a 0.8 cm diameter. The optical properties of this finger phantom are chosen to closely resemble those typically found in and around the proximal interphalangeal (PIP) joint of the human hand (Table 3), resembling clinical applications for the diagnosis of rheumatoid arthritis [17].

The cross-sectional maps of the reconstructed absorption and scattering coefficients are presented in Fig. 16. As shown in Fig. 16, the SP_3 algorithm performs better than the SP_1 algorithm in both locating the inclusions and reconstructing the actual values of absorption and scattering there in the region of inclusions. In terms of image quality, the correlation coefficient ρ of the SP_3 model is 0.66 for μ_a reconstruction and 0.64 for μ_s' reconstruction. This is almost 20%–40% better than when the SP_1 model is used ($\rho(\mu_a) = 0.46$ and $\rho(\mu_s') = 0.20$, respectively). Also the SP_3 method shows 80%–250% smaller deviation factors ($\delta(\mu_a) = 0.77$ and $\delta(\mu_s') = 0.82$) as compared to the SP_1 method ($\delta(\mu_a) = 1.60$ and $\delta(\mu_s') = 3.40$). Overall, the SP_1 reconstructions give highly overestimated results, causing greater artifacts in the region where the sources are located, whereas the SP_3 estimates the optical properties more accurately with much less artifact in the same region. The main reason that the SP_3 outperform the SP_1 reconstruction for this case is because the SP_3 forward model gives better predictions of light intensities near the source locations than the SP_3 as described in sec. 4.1. Convergence characteristics for this case are shown in Fig. 17 for the two algorithms. The SP_1 method reveals much larger initial error and converges at larger value, not making further progress toward the minimum whereas the SP_3 method converges at smaller value by two orders of magnitude. In terms of CPU times, the SP_3 method takes about 60% more time than the SP_1 method when the algorithms are terminated after 22 inverse iterations.

6. Conclusions

We introduce here the finite volume approximation to the FD-SP_3 model with strictly real-valued nth order absorption coefficients and then present the FD-SP_3 based reconstruction

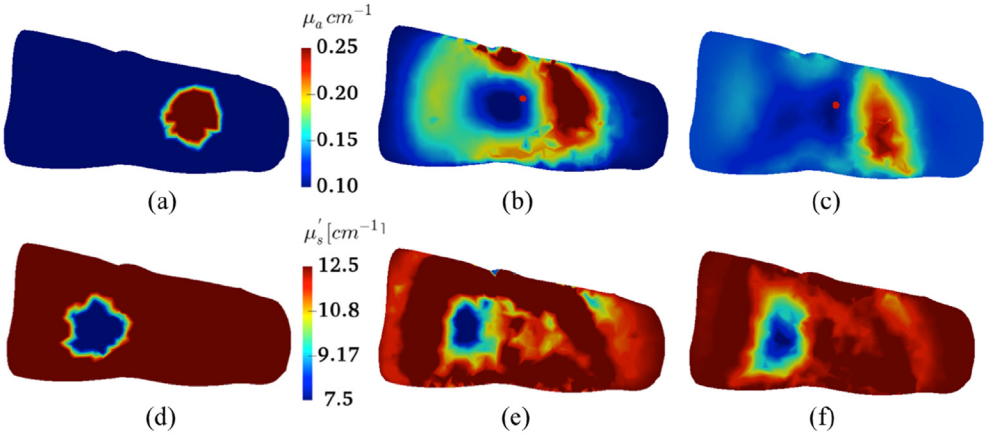

Fig. 16. Sagittal cross-sectional views of the 3D finger phantom, showing the absorption μ_a (top) and scattering μ_s' (bottom) obtained with SP_1 and SP_3: (a,d) exact; (b,e) SP_1; (c,f) SP_3.

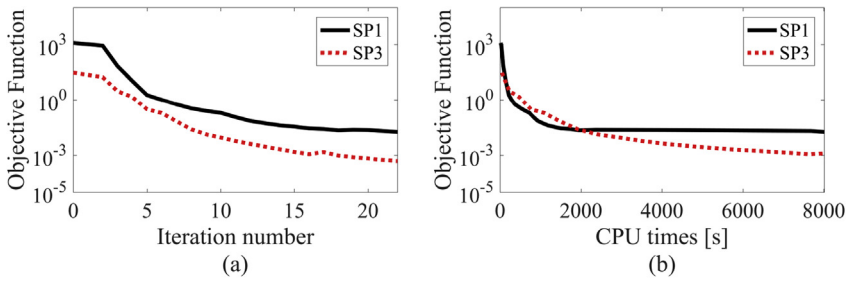

Fig. 17. Convergence of the reconstruction algorithms with respect to (a) iteration number and (b) time.

algorithm for recovering absorption and scattering coefficients in biological media. The FD-SP_3 model is discretized with a node-centered finite volume scheme. The resulting system of linear algebraic equations is solved with restarted generalized GMRES algorithm. The absorption and scattering coefficients are recovered using the quasi-Newton limited-memory BFGS algorithm, in which the gradient of the objective function is computed using exact differentiation with respect to μ_a and μ_s. Finally, the forward and inverse algorithms are validated using numerical phantoms with optical properties that mimic biological tissue. The forward solutions are compared to the solutions obtained from the ERT (S_{12}) model.

The results with the forward models show that the FD-SP_3 approximates the FD-ERT model to within reasonable accuracy. We find that the second composite moment of the fluence, ϕ_2, corrects the first moment of the fluence, ϕ_1, near the location of the source and in the areas where the inclusions exist. This is in accordance with our expectations, as it is well known that incoming photons do not become diffuse until they travel a short distance within media with high absorbing and scattering properties. Thus, the SP_3 solution is able to better approximate the "transport" behavior of photons at short distances from the source.

From the reconstruction results presented here we find that the absorption and scattering coefficient maps are more accurately reconstructed with the SP_3 model than with the SP_1 model while the SP_3 model takes fewer iterations to converge. These convergence properties result in reducing the overall difference in reconstruction time between the SP_1 and SP_3 models.

Overall, this work shows that the FV-FD-SP_3 is a computationally efficient model for DOT imaging of media with non-diffuse properties, such as finger joints, because it performs better than the SP1 (i.e., diffusion model) with respect to accuracy and takes significantly lower computation time than the FD-ERT (S_{12}) model without sacrificing accuracy significantly. Our future effort will focus on deploying this algorithm for use in clinical data with the aim of diagnosis of rheumatoid arthritis from FD-DOT imaging of finger joints.

Acknowledgements

This work was supported in part by grants from the National Institute of Arthritis and Musculoskeletal and Skin Diseases (NIAMS 5R01AR050026) and the National Heart, Blood, and Lung Institute (NHLBI-1R01-HL115336), which are both part of the National Institutes of Health (NIH). Furthermore, support was provided partially by a NIAMS training grant on "Multidisciplinary Engineering Training in Musculoskeletal Research" (5 T32 AR059038 02).

References

[1] Prahl SA, Keijzer M, Jacques SL, Welch AJ. A monte carlo model of light propagation in tissue. Proc SPIE IS 1989;5:102–11.
[2] Wang L, Jacques SL, Zheng L. Mcml–monte carlo modeling of light transport in multi-layered tissues. Comput Methods Programs Biomed 1995;47(no. 2):131–46.
[3] Fang Q, Boas DA. Monte carlo simulation of photon migration in 3d turbid media accelerated by graphics processing units. Opt Express Oct 2009;17:20178–90.
[4] Patterson MS, Chance B, Wilson BC. Time resolved reflectance and transmittance for the non-invasive measurement of tissue optical properties. Appl Opt Jun 1989;28:2331–6.
[5] Arridge SR, Cope M, Delpy DT. The theoretical basis for the determination of optical pathlengths in tissue: temporal and frequency analysis. Phys Med Biol 1992;37(no. 7):1531.
[6] Arridge SR, Schweiger M, Hiraoka M, Delpy DT. A finite element approach for modeling photon transport in tissue. Med Phys 1993;20(no. 2):299–309.
[7] Hielscher AH, Alcouffe RE, Barbour RL. Comparison of finite-difference transport and diffusion calculations for photon migration in homogeneous and heterogeneous tissues. Phys Med Biol 1998;43(no. 5):1285.
[8] Dorn O. A transport-backtransport method for optical tomography. Inverse Probl 1998;14(no. 5):1107.
[9] Klose AD, Hielscher AH. Iterative reconstruction scheme for optical tomography based on the equation of radiative transfer. Med Phys 1999;26(no. 8):1698–707.
[10] Klose AD, Netz U, Beuthan J, Hielscher AH. Optical tomography using the time-independent equation of radiative transfer – part 1: forward model. J Quantitative Spectrosc Radiat Transf 2002;72(no. 5):691–713.
[11] Ren K, Abdoulaev GS, Bal G, Hielscher AH. Algorithm for solving the equation of radiative transferin the frequency domain. Opt Lett Mar 2004;29:578–80.
[12] Salah MB, Askri F, Nasrallah SB. Unstructured control-volume finite-element method for radiative heat transfer in a complex 2-d geometry. Numer Heat Transf Part B Fundam An Int J Comput Methodol 2005;48(no. 5):477–97.
[13] Kim HK, Hielscher AH. A pde-constrained sqp algorithm for optical tomography based on the frequency-domain equation of radiative transfer. Inverse Probl 2009;25(no. 1):015010.
[14] Klose AD. "Radiative transfer of luminescence light in biological tissue," in Light Scattering Reviews 4. In: Kokhanovsky AA, editor. Springer praxis books. Berlin Heidelberg: Springer; 2009. p. 293–345.
[15] Arridge SR, Schotland JC. Optical tomography: forward and inverse problems. Inverse Probl 2009;25(no. 12):123010.
[16] Ren K, Bal G, Hielscher AH. Transport- and diffusion-based optical tomography in small domains: a comparative study. Appl Opt Sep 2007;46:6669–79.
[17] Hielscher A, Kim HK, Montejo L, Blaschke S, Netz U, Zwaka P, et al. Frequency-domain optical tomographic imaging of arthritic finger joints. Med Imaging 2011;30:1725–36. IEEE Transactions on.
[18] Montejo LD, Jia J, Kim HK, Netz UJ, Blaschke S, M üller GA, et al. Computer-aided diagnosis of rheumatoid arthritis with optical tomography, part 1: feature extraction. J Biomed Opt 2013;18(no. 7):076001.
[19] Montejo LD, Jia J, Kim HK, Netz UJ, Blaschke S, M üller GA, et al. Computer-aided diagnosis of rheumatoid arthritis with optical tomography, part 2: image classification. J Biomed Opt 2013;18(no. 7):076002.
[20] Yuan Z, Zhang Q, Sobel E, Jiang H. Three-dimensional diffuse optical tomography of osteoarthritis: initial results in the finger joints. J Biomed Opt 2007;12(no. 3):034001.
[21] Yuan Z, Zhang Q, Sobel E, Jiang H. Comparison of diffusion approximation and higher order diffusion equations for optical tomography of osteoarthritis. J Biomed Opt 2009;14:054013.
[22] Yuan Z, Zhang Q, Sobel ES, Jiang H. High-resolution x-ray guided three-dimensional diffuse optical tomography of joint tissues in hand osteoarthritis: morphological and functional assessments. Med Phys Aug 2010;37:4343–54.
[23] Klose AD, Larsen EW. Light transport in biological tissue based on the simplified spherical harmonics equations. J Comput Phys 2006;220(no. 1):441–70.
[24] Morton K, Mayers D. Numerical solution of partial differential equations: an introduction. Numerical solution of partial differential equations: an introduction. Cambridge University Press; 2005.
[25] Dom ınguez JB, erub e-Lauzi'ere YB. Diffuse light propagation in biological media by a time-domain parabolic simplified spherical harmonics approximation with ray-divergence effects. Appl Opt Mar 2010;49:1414–29.
[26] Boas D, Pitris C, Ramanujam N. Handbook of biomedical optics. Taylor & Francis; 2011.
[27] Chu M, Vishwanath K, Klose AD, Dehghani H. Light transport in biological tissue using three- dimensional frequency-domain simplified spherical harmonics equations. Phys Med Biol 2009;54(no. 8):2493.
[28] Lu Y, Zhu B, Shen H, Rasmussen JC, Wang G, Sevick-Muraca EM. A parallel adaptive finite ele- ment simplified spherical harmonics approximation solver for frequency domain fluorescence molecular imaging. Phys Med Biol 2010;55(no. 16):4625.
[29] Minkowycz W, Sparrow E, Murthy J. Handbook of numerical heat transfer. Wiley; 2006.
[30] Saad Y, Schultz MH. Gmres: a generalized minimal residual algorithm for solving nonsymmetric linear systems. SIAM J Sci Stat Comput 1986;7(no. 3):856–69.
[31] Liu DC, Nocedal J. On the limited memory bfgs method for large scale optimization. Math Program 1989;45:503–28. http://dx.doi.org/10.1007/BF01589116.
[32] Saad Y. Iterative methods for sparse linear systems. second ed. Society for Industrial and Applied Mathematics; 2003.
[33] Ren K, Bal G, Hielscher AH. Frequency domain optical tomography based on the equation of radiative transfer. SIAM J Sci Comput Apr. 2006;28:1463–89.
[34] Alifanov OM. Inverse heat transfer problems. New York: Springer- Verlag; 1994.
[35] Nocedal, Wright S. Numerical optimization. Springer series in operations Research and financial engine. Springer Science+Business Media, LLC; 2006.